Improving the Bulk Gas Transport of Fe-N-C Platinum Group Metal-free Nanofiber Electrodes via Electrospinning for Fuel Cell Applications

Sadia Kabir,[a] Samantha Medina,[b] Guanxiong Wang,[a] Guido Bender,[a] Svitlana Pylypenko [a, b,+] and K.C. Neyerlin[a,+]

[a]National Renewable Energy Laboratory, Golden, CO 80401, USA.

[b] Colorado School of Mines, Golden, CO 80401

[a,+] Corresponding Authors: Kenneth.Neyerlin@nrel.gov, spylypen@mines.edu

Abstract

To overcome transport limitations associated with thicker platinum group metal-free (PGM-free) electrodes, it's imperative to investigate and tailor alternative electrode architectures to maximize the bulk electrode transport properties, whilst not significantly impeding electrocatalyst active site accessibility and electrode proton resistance. In this work, PGM-free nanofiber electrode mats, prepared by electrospinning a mixture of pyrolyzed Fe-N-C catalyst, Nafion ionomer and a carrier polymer Poly Acrylic acid (PAA), were compared to traditionally prepared electrodes. The morphological properties and elemental distribution of the fabricated nanofiber electrodes showed that the exterior surface of the PGM-free nanofibers was conformally covered with a thin ionomer film. Electrochemical diagnostics performed utilizing cyclic voltammetry, electrochemical impedance spectroscopy (EIS) and H_2-limiting current measurements, revealed an increase in electric double layer capacitance, reduction in electrode proton transport and a significant improvement in bulk-electrode gas transport properties for the nanofiber electrodes, supporting the observed performance increase from electrochemical polarization data obtained in

H_2-O_2/Air fuel cells. At 100% RH in H_2/Air, the power density of the nanofiber electrodes increased ca. 50% vs. the traditionally prepared electrodes (ca. 260 vs 175 mW cm^{-2}), which was attributed to a less tortuous molecular diffusion pathway and an associated reduction in the pressure dependent and independent gas transport resistances in the nanofiber electrodes.

TOC

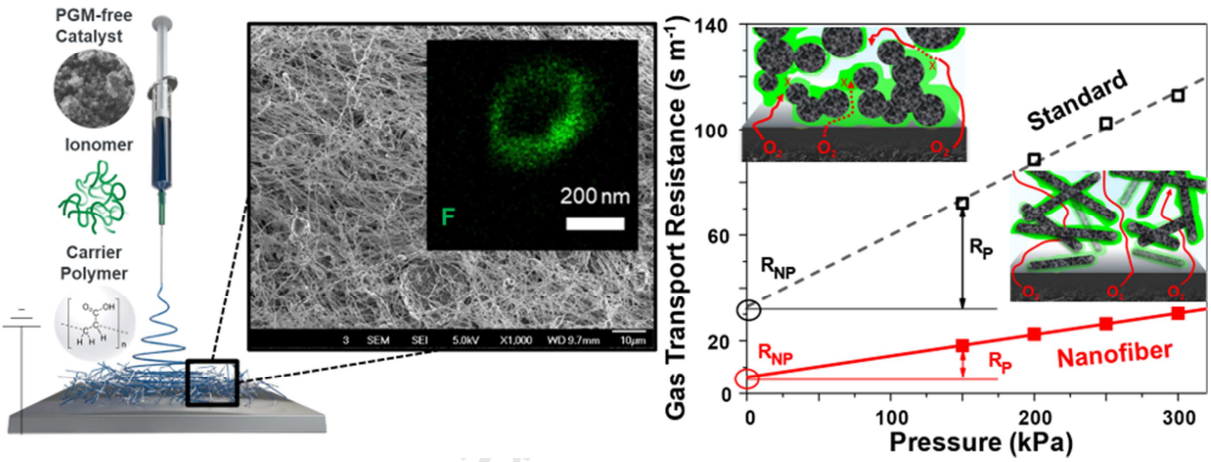

Keywords

Fuel cells, PGM-free electrode, nanofiber, electrospinning, proton transport, gas transport

1. Introduction.

Fuel cells are considered to be one of the most promising sustainable energy technologies for electric power generation due to their high electrical efficiencies, low operating temperatures and zero tailpipe emissions, making them ideal candidates for both transportation and residential applications.[1,2] To date, polymer electrolyte membrane fuel cells (PEMFCs) have heavily relied on platinum and platinum group metal (PGM) electrocatalysts for catalyzing the hydrogen oxidation and sluggish oxygen reduction reactions (ORR).[3–6] However, even at high volume

production (>500,000 stacks) PGM electrocatalysts account for 42% of the PEMFC stack cost, hindering wide scale implementation in the automotive sector.[7] Therefore, the U.S. Department of Energy (DOE) has promoted a parallel pursuit of high-performing PGM-free electrocatalysts and electrodes[8] in order to reduce automotive system cost to the $30/kW cost target,[9,10] and ultimately improve the cost-competitiveness of fuel cells in a wide range of applications.

Low cost earth-abundant PGM-free ORR electrocatalysts have been extensively studies over the past decade and a half, towards reducing and eliminating the use of precious metals at the cathode side.[11] Most PGM-free ORR electrocatalysts consist of nitrogen-functionalized (N_x) transition metals (TM = Fe, Co, Ni) embedded in a mesoporous carbon (C) matrix, i.e. TM–N_x/C.[12–14] PGM-free catalysts are generally derived from high temperature treatment of transition metal precursors and nitrogen sources, zeolitic imidazolate frameworks (ZIFs) and porous organic polymers (POPs)[15–18] and have demonstrated promising activities in both acidic and alkaline media.[19–21] While a variety of new synthetic approaches continue to be explored, [22–24] and remarkable progress has been made in synthesizing highly active TM-N_x/C electrocatalysts,[8,25] significant R&D barriers still remain at both the electrocatalyst and electrode levels.[26]

PGM and PGM-free electrodes are usually prepared by conventional methods such as painting, airbrushing or via ultrasonic spray-coating.[27,28] However, due to the relatively lower active site density and turn-over frequency (TOF) in TM-N_x/C catalysts,[25,29] PGM-free catalyst layers are typically an order of magnitude thicker (70 - 120 μm) when compared to commercial Pt/C electrodes (~5-10 μm).[30] The higher loaded, thicker PGM-free electrodes come with additional obstacles, namely additional O_2 transport through the bulk of the electrode structure as well as an increased proton transport resistance.[31–34] Consequently, alternative electrode

fabrication strategies that can manipulate ionic and gas phase transport are imperative for investigating and optimizing PGM-free electrode structures.

Electrospinning has been shown to enable the fabrication of 3-dimensional PGM-free electrode architectures with varying degrees of porosity,[35] along with purported improvements in stability along with higher power densities in H_2/Air fuel cells.[36,37] Although these results are promising, no direct measurement of the improved device level transport properties for PGM-free nanofiber electrodes currently exists. Elucidating the transport resistances stemming from bulk-electrode gas (through the thickness of the electrode) and proton transport at the MEA level along with a subsequent correlation to MEA performance will help identify limiting phenomena and pathways to improve PGM-free electrocatalyst integration. Such mitigation will require an understanding of ionomer distribution, active-site accessibility, electrode proton conduction and quantification of gas transport resistance.

This study focuses on the use of various microscopic and electrochemical diagnostics to provide a detailed understanding of morphological and electrochemical properties of PGM-free nanofiber electrodes. Here, a nanofiber electrode fabricated from a solution of nicarbazin-derived Fe-N-C PGM-free catalyst (Pajarito Powders LLC), D2020 Nafion ionomer and carrier polymer poly acrylic acid (PAA) is compared to a standard electrode prepared by hand painting. Both electrodes were then tested in H_2-O_2/Air fuel cells under a range of operating conditions. The electrochemical performance data is contrasted with cyclic voltammetry, H_2-limiting current and electrochemical impedance spectroscopy to characterize; i) capacitive behavior as a function of relative humidity, gleaning potential information about ionomer distribution and active site accessibility, ii) bulk electrode gas transport resistance, and iii) electrode proton transport resistance, respectively.

2. Experimental Methods.

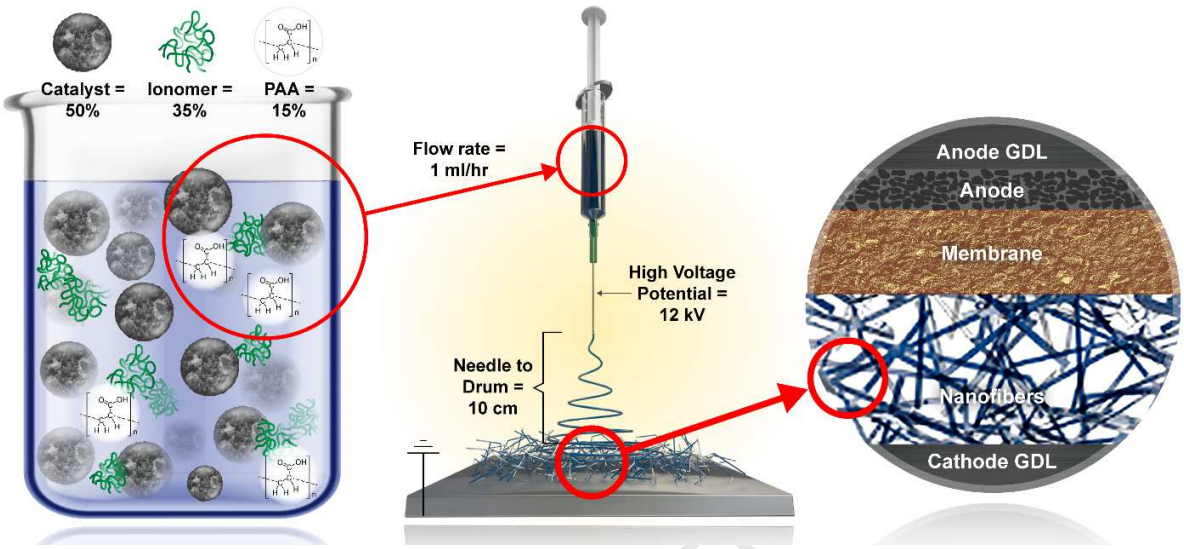

Figure 1. **Schematic illustration of (a) PGM-free electrospun ink formulation comprising of Fe-N-C Catalyst : Ionomer : PAA homogenized mixture, (b) the electrospinning apparatus for creating the PGM-free nanofiber electrode mat and (c) MEA fabrication with PGM-free nanofiber mat as hot-pressed cathode CCL and Pt/HSC anode GDE.**

2.1 PGM-free Nanofiber Electrospun Electrode

2.1.1 Electrospun Ink Formulation. The ink for electrospinning comprised of (a) Nicarbazin-derived Fe-N-C PGM-free electrocatalyst, (b) D2020 Nafion ionomer as received from Ion Power and (c) poly(acrylic acid) – PAA 450 kDa molecular weight from Sigma Aldrich (Fig. 1a). The ink was prepared by mixing a 50:35:15 (wt.%) ratio of catalyst : ionomer : PAA in a 1:1 (wt.%) solvent/de-ionized water solution of IPA and Water with an ionomer: carbon (I:C) wt.% ratio of 0.7. The catalyst powders were ball milled and the inks were homogenized by the following three-step procedure: (1) a dispersion of ball milled PGM-free catalyst powder in 1:1 (w/w) IPA:Water solvent and D2020 Nafion was ultrasonically agitated via tip sonication

for 30 mins, (2) followed by an additional 60 minutes of bath sonication. Once bath and horn sonicated, (3) a solution of PAA (7.5 wt.% in IPA:Water) was added to the catalyst and ionomer ink mixture followed by atleast 48 hours of mechanical stirring.

2.1.2 Electrospinning Parameters and Nanofiber CCL Fabrication. The ink was drawn into a 20 mL syringe and electrospun using a stainless steel 22 gauge needle spinneret. (Fig. 1b) The needle tip was polarized to a potential of 12 kV relative to a grounded stainless steel rotating and laterally oscillating aluminum foil covered drum collector that was operated at a rotation speed of 100rpm. The spinneret-to-collector distance was fixed at 10 cm and the flow rate of ink was held constant for all experiments at 1 mL/h. Electrospinning was performed at room temperature in a custom-built environmental chamber, where the relative humidity was maintained between 35-40 % RH. At the end of the experiment, the nanofibers were collected from the aluminum foil, weighed to confirm a catalyst-only loading of 3 mg cm^{-2}, and then and hot pressed onto a NRE211 Membrane under 1800 kg, 140°C for 2 mins. (Fig. 1c). The thickness of the nanofiber electrodes (50-70 µm) was verified with a micrometer.

2.3 Standard Electrode. For fabricating a standard conventional electrode, 42 wt.% of ball milled PGM-free catalyst powder was mixed with 58 wt.% of Nafion ionomer (5 wt.% 1100 EW LIQUION from Ion Power) in a 1:1 (wt.%) de-ionoized water:IPA solvent mixture with a concentration of 25.6 mg/ml. Similar to the electrospun ink, the standard ink was also formulated to have a ionomer/carbon (I/C) ratio of 0.7. Following 2 hours of bath sonication, the standard PGM-free electrode was then prepared by coating the ink onto the cathode side of the membrane with a brush under a vacuum sealed plate at 95°C with a loading of 3 mg cm^{-2}. This loading was verified based on ink composition, concentration, and volume used for hand painting the electrode, as well as catalyst layer thickness, (~40 µm) verified with a micrometer.

2.4 Anode Fabrication. The anode ink consisted of a mixture of deionized water and n-propanol (at a weight ratio of ~6:4), ionomer (D2020 20 wt.% Nafion from Ion Power), and 50 wt.% Pt/HSC from Umicore. The ionomer, solvent and catalyst mixture were horn sonicated for 20 s to break up carbon agglomerates, followed by bath sonication for 20 min. Both sonication steps were done with the ink submerged in an ice bath. All the anodes inks were coated in-house using a Sono-Tek ultrasonic spray coating system (Exacta Coat model) equipped with a 25 kHz Accumist nozzle with a loading of 0.10 mg_{Pt} cm^{-2}.

2.5 Fuel Cell Performance Testing. The standard and nanofiber CCMs were sandwiched between two 5 cm^2 SGL29 BC gas diffusion layers (GDLs) at 25% compression and assembled into 5 cm^2 hardware for fuel cell testing. The CCMs, GDLs, and polytetrafluoroethylene (PTFE) gaskets were then placed between the flow fields and the bolts tightened to 40 inch-pounds. Once assembled, a break-in procedure was first implemented by heating the cell to 80°C and holding the cell at 0.4 V under H_2/O_2 (0.3/0.3 SLPM, respectively) at 150% RH and 150 kPa till the current stabilized. H_2/O_2 and H_2/Air polarization curves were then obtained from 0.1 V to OCV at 80^{o}C, 100 kPa O_2 partial pressure (150 kPa_{abs} cell pressure) and 100 % RH for 4 minutes per point (average of last 1 min. used) in the anodic direction. Following the polarization curves taken at 100% RH, additional polarization curves were also taken at lower relative humidity ranging from 75 - 50% RH at 80°C and 150 kPa_{abs}.

2.6 Electrochemical Impedance Spectroscopy and Cyclic Voltammetry. Metrohm Autolab 302N potetiostat/galvanostat was used for collecting all the electrochemical impedance spectroscopy (EIS) and cyclic voltammetry data as a function of relative humidity. EIS was performed by sweeping from 10 kHz – 0.1 Hz using a sinusoidal perturbation amplitude equal to 5 mV in the case of H_2/N_2 EIS and perturbation amplitude equal to 5% of DC current in the case

of H_2/H_2 EIS. Cyclic voltammograms were then performed under H_2/N_2 sweeping from 0.01 to 1.2 V vs. RHE at 20 mV/s at 100, 75, 50 and 20% RH. The geometric electrode capacitance was determined using a H2-fed anode reference/counter electrode and a N_2-purged cathode working electrode. CVs were then recorded between 0.01 – 1.0 V vs. RHE and the current obtained was then divided by the applied potential scan rate (20 mV s^{-1}) to determine the capacitive response in mF cm^{-2} as a function of relative humidity, ranging from 25% RH to 100% RH.

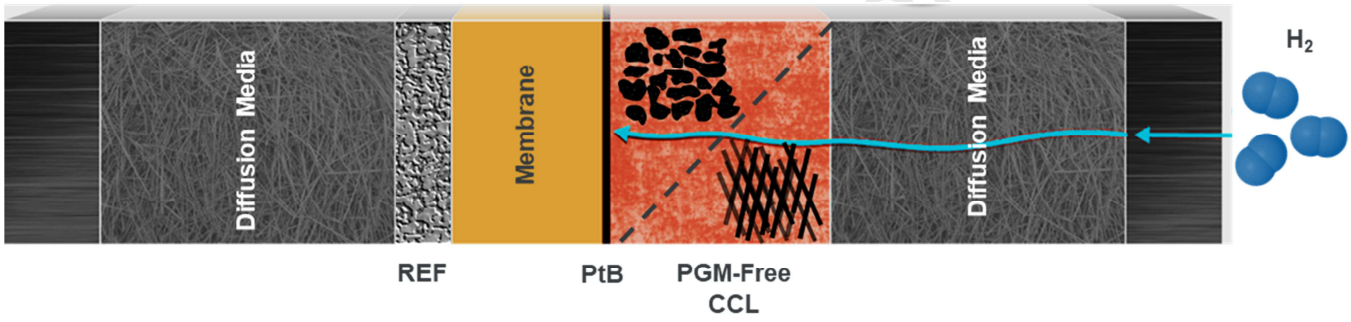

Figure 2. **Schematic illustrating the components in a MEA fabricated for bulk electrode transport measurement using H_2-limiting current diagnostics. The PGM-free catalyst layer (comprising of either nanofibers or standard ink) is deposited on the Platinum black sensor (PtB) and H_2-limiting currents are measured at the Pt/B and PGM-free CCL interface for elucidating gas transport resistances in the PGM-free CCLs.**

2.7 Bulk Electrode Transport Measurements. Identical to what was previously published,[34,38] all cells were fabricated using Nafion 211 membranes (DuPont) and 060 carbon paper diffusion media with 5% wet-proofing (Toray). All electrodes were deposited with a Sonotek ExactaCoat OP3 ultrasonic spray station in an alternating horizontal and vertical raster pattern. Platinum black (PtB) sensor layers were fabricated from inks of 4:3 ratio deionized water to n-propanol with catalyst mass concentration of 4 $mg_{catalyst}/mL_{ink}$. PtB layer catalyst loadings were ~0.8 mgPt

cm^{-2} verified by X-ray Fluorescence Spectroscopy (XRF) on a Fisher XDV-SDD. The PtB inks excluded ionomer because testing showed no proton transport limitations. This also avoided the possibility of PtB poisoning via sulfonate side-chain adsorption. Reference electrodes (REF) were fabricated from inks containing platinum on high surface area carbon (TEC10E50E, TKK) with 5 wt% Nafion ionomer dispersion (DuPont DE2020, Ion Power) at 0.9 ionomer to carbon ratio and 4:3 ratio deionized water to n-propanol. Nominal REF catalyst loadings were 0.2 mg_{Pt} cm^{-2} also verified by XRF. PGM-free CCL were than deposited on the PtB sensor by (a) hot-pressing 3 mg cm^{-2} of the Fe-N-C nanofiber mat at 1800 kg, 140°C for 2 mins or (b) coating a mixture of the standard ink formulation with a paint brush described in section 2.3. H_2 Limiting currents were measured by cyclic voltammetry (CV) with 5% H_2 balance N_2 at both the working PtB layer and REF electrodes (to limit hydrogen crossover). Three sweeps were collected and the maximum current of the third sweep, undifferentiated from the second sweep was the limiting current value (after corrections for hydrogen crossover and background capacitance). Background CVs were collected under 5% H_2/N_2 in the anode and cathode. A Teledyne Medusa test stand controlled cell temperature, pressure, gas flows, and inlet gas humidity.

2.8 Electron Microscopy Methods. Secondary electron images (SEI) of the PGM-free catalyst and nanofiber mats were obtained with a JEOL 7000F FE-SEM operating at a 5kV accelerating voltage and a 10 mm working distance. The catalyst powder and nanofibers were placed on double sided carbon tape and on a flat specimen holder prior to imaging. The individual PGM-free nanofibers were placed directly on a SPI Supplies Slim-Bar 400 mesh copper grid, for transmission electron microscopy (TEM) analysis with an FEI Talos F200X electron microscope operating at 200 keV. Energy dispersive spectroscopy (EDS) was acquired using the scanning TEM (STEM) mode, with both bright field (BF) and high angle annular dark field (HAADF)

image production. Further analysis was conducted on cross-sections of nanofibers prepared via ultramicrotomy. The fibers were embedded in Araldite 6005 epoxy resin mixture and cured at 60°C for 16 hours, followed by trimming and ultramicrotomy using a 36° clearance angle Diatome diamond knife. The fiber cross-sections were approximately 100 nm thick making them electron transparent for STEM analysis.

3. Results and Discussion.

3.1 Physicochemical characterization of PGM-free Nanofibers.

3.1.1 Morphology.

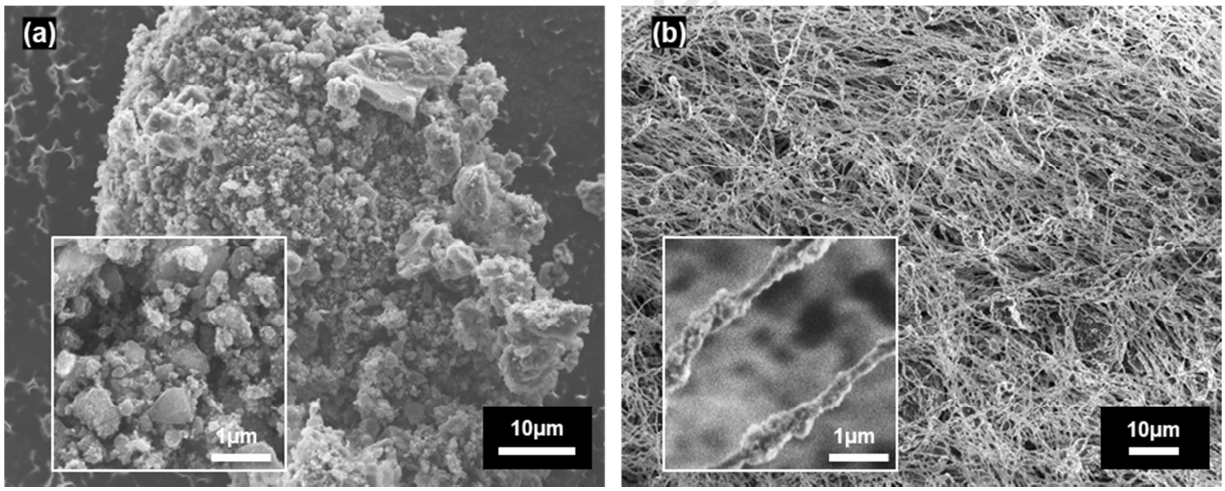

Figure 3. **SEM micrographs of (a) PGM-free catalyst powder with inset showing the primary particles and (b) PGM-free fiber mat with inset showing a higher magnification image of the nanofiber morphology.**

Fig. 3a shows an SEM image of the catalyst powder, with particle agglomerates ranging from 5-15 um, while Fig. 1b displays SEM micrographs of a networked structure of PGM-free nanofibers with 0.5-5 μm size voids throughout the fiber mat. The inset in Fig. 1a is a higher

magnification image, illustrating primary particles ranging between 0.1 to 1 μm. These larger agglomerated particles, however, are not seen in the nanofiber (inset in Fig. 1b), suggesting that shearing/mixing events during electrospinning increase the break-up of large catalyst agglomerates.

Recent studies have shown that smaller catalyst aggregates in standard electrodes result in smaller pores and a lower effective diffusion coefficient for the bulk electrode structure in PGM-free electrodes.[39] However, the key component here is that while electrospinning provides smaller catalyst aggregates, this method of integration allows for large continual macropores throughout the bulk electrode structure, while traditional fabricated electrodes do not.

3.1.2 Elemental Composition.

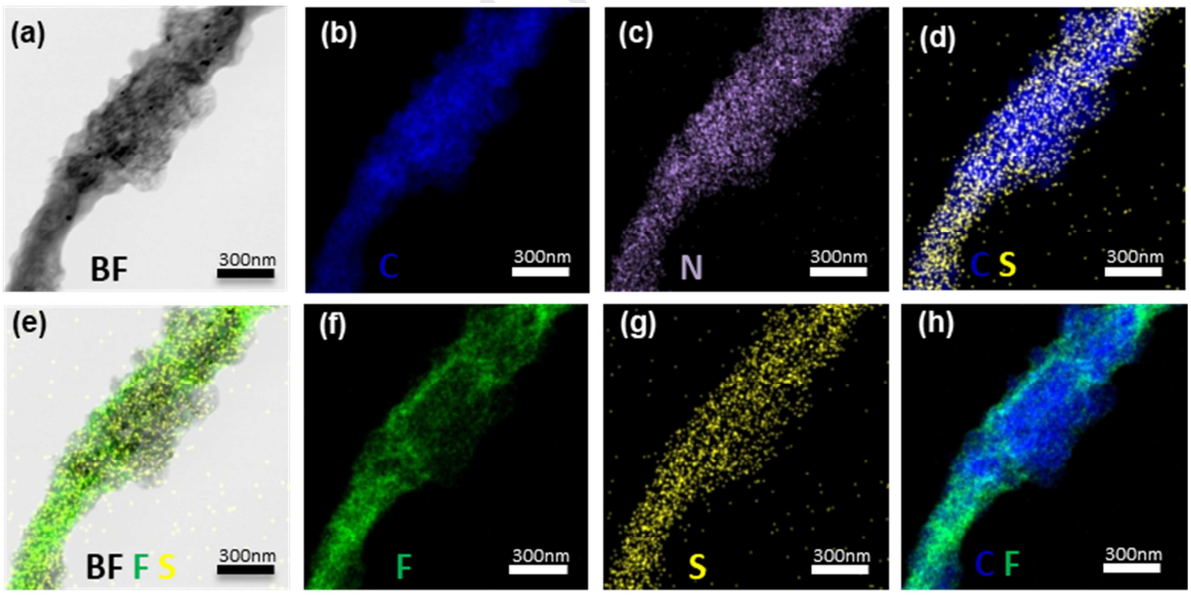

Figure 4. **STEM BF image showing the nanofiber morphology and thickness variation (a), and EDS maps showing the elemental distribution of, (b) carbon, C-blue (c) nitrogen, N-purple (d) carbon and sulfur overlay, C-blue and S-yellow, (e) STEM BF image with**

fluorine and sulfur overlays, F-green and S-yellow, (f) fluorine, F-green, (g) sulfur, S-yellow, (h) carbon and fluorine overlays, C-blue and F-green.

TEM images of the individual Fe-N-C PGM-free fibers were obtained to assess ionomer distribution along the fiber, which was fabricated with a 50:35:15 Fe-N-C Catalyst : Nafion : PAA wt.%. The bright field image in Fig. 4a shows a representative nanofiber with a diameter between 250 and 500 nm. A certain level of intra-fiber micro-porosity is observed, with PGM-free catalyst aggregates embedded within the fiber diameter. Elemental maps of F, S and C in Fig. 2-b, f, and g using STEM-EDS indicate a nearly complete distribution of carbon, with a well distributed, though discontinuous ionomer phase. An elemental map of the entire fiber mat is also shown in Fig. S1 and confirms that it is comprised of an Fe-N-C catalyst.

3.3 Fuel Cell performance of PGM-free Nanofiber Electrodes vs. Standard Electrodes.

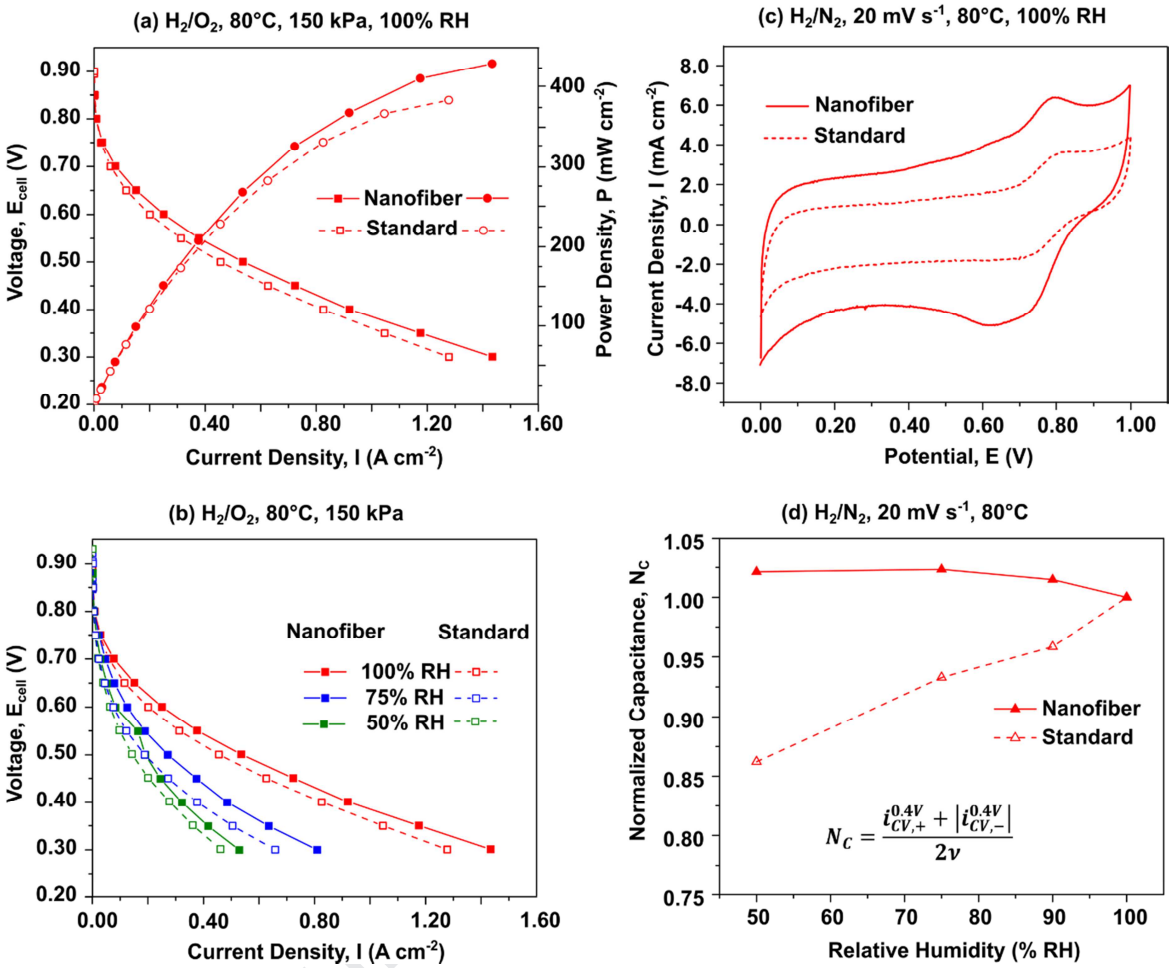

Figure 5. (a) **Fuel cell polarization curves for 5 cm^2 MEAs with PGM-free (■) nanofiber and (□) standard electrodes with a loading of 3 mg cm^{-2} fabricated via electrospinning and conventional hand painting. The cells were operated in H_2/O_2 at 80°C, 150 kPa, and 100% RH and (b) 50, 75 and 100% RH. (c) Cyclic voltammograms of standard and nanofiber electrodes obtained at 100% RH in H_2/N_2 at 20 mV s^{-1}. (d) Normalized capacitance of the nanofiber and standard electrodes estimated form CVs measured from 100-50% RH.**

Fig. 5a and 5b show the performance of standard and PGM-free nanofiber electrodes (cathode loading of 3 mg·cm^{-2}) in 5 cm^2 single-cell H_2-O_2/air fuel cells. Under fully-humidified

conditions (100% RH), the nanofiber MEA demonstrated improved performance in comparison to the standard MEA. Moreover, the PGM-free nanofiber electrode attains a peak power density of 430 mW cm^{-2} whereas the standard electrodes reach only a peak power density of ~383 $mW \cdot cm^{-2}$. The H_2/O_2 polarization measurements obtained between 75-50% RH conditions also show an improved performance of the nanofiber electrodes under "drier" conditions.

The higher H_2/O_2 MEA performance metrics can be attributed to a combination of factors such as high active site density, accessibility to electrochemically active sites, and others. The electrochemical double layer (EDL) capacitance of the electrodes can provide further insights into the active site accessibility within the catalyst layers via cyclic voltammetry (CV) measurements.[40] The measured capacitance can then be utilized for a qualitatively estimating the accessibility of active sites during ORR, as well as the dependence of ionic conductivity as a function of capacitance on the applied potential and testing conditions, such as relative humidity.

Fig. 5c shows the capacitive behavior of standard and the nanofiber electrodes under fully humidified conditions. A characteristic feature, particularly the broad oxidation peaks observed ca.~0.7 V from the CV's of the nanofiber is related to the pseudocapacitive behavior due to faradaic redox reactions of active elements in the Fe-N-C moieties.[41] The peaks corresponding to the redox couples generically referenced as Fe^{2+}/Fe^{3+} more prevalently in the literature,[42] but more recent works have shown that the ligands, which surround the atomically dispersed centers may affect the oxidation state of the metal center, and result in a non-integer value for the oxidation state (Fe^{LO}/Fe^{HO}), since oxidation states can themselves vary.[43] Nevertheless, the transition from Fe^{HO} to Fe^{LO} has been purported to be associated with the availability/activity of the PGM-free active site, which is more prominent in the nanofiber electrode as compared to standard electrode.

The increased capacitance most likely results from the increased break-up of large aggregates due to particle shearing under the applied electric field during the electrospinning process (Fig. 3b). The increased capacitance for nanofiber electrodes implies improved access to electrochemical active sites, as is shown by the improvements in low current density (high potential) performance in Fig. 5b, even at low RH. The increased intra-fiber and/or inter-fiber voids, as seen in MEA cross sections in the fiber electrodes, (Fig. S2) will also allow for a facile O_2 access to the active sites.

Understanding active site accessibility is also important for understanding PEMFC performance under both wet and dry conditions under a range of operating conditions. Studies have shown that the exposure of ionomer films to liquid water can alter its structure and hydrophilicity,[44] which affects its ability to provide adequate ionic contact to shuttle protons to and from active sites and qualitatively reflect the accessibility of active sites as a function of water content (i.e. RH). and capacitance. This variation in ionic accessibility to active sites will vary depending on the geometry and distribution of the ionomer within the catalyst layers, which can be qualitatively measured using cyclic voltammetry.

Fig. 5d shows the normalized capacitance (N_C) of the standard and nanofiber electrodes obtained at as a function of RH (Fig. S3), where ν is the scan rate, and $i_{CV,+}^{0.V}$ and $i_{CV,}^{0.V}$ are the current density measured at 0.4 V in the positive and negative scan directions, respectively.

$$c = \frac{i_{CV,+}^{0.4V} + \left| i_{CV,-}^{0.4V} \right|}{2\nu} \qquad [1]$$

The normalized capacitance of the standard electrode shows a clear dependence on RH, resulting from both improved ionomer/electrocatalyst interactions with increased water uptake along with enhanced capillary condensation as electrocatalyst and electrode micro and meso-pores become

filled with liquid water. In contrast, the N_C of the nanofiber electrode is largely independent of RH from 50-100% (within confidence of the measurement), implying that the ionomer is well distributed near the electrocatalyst surface.

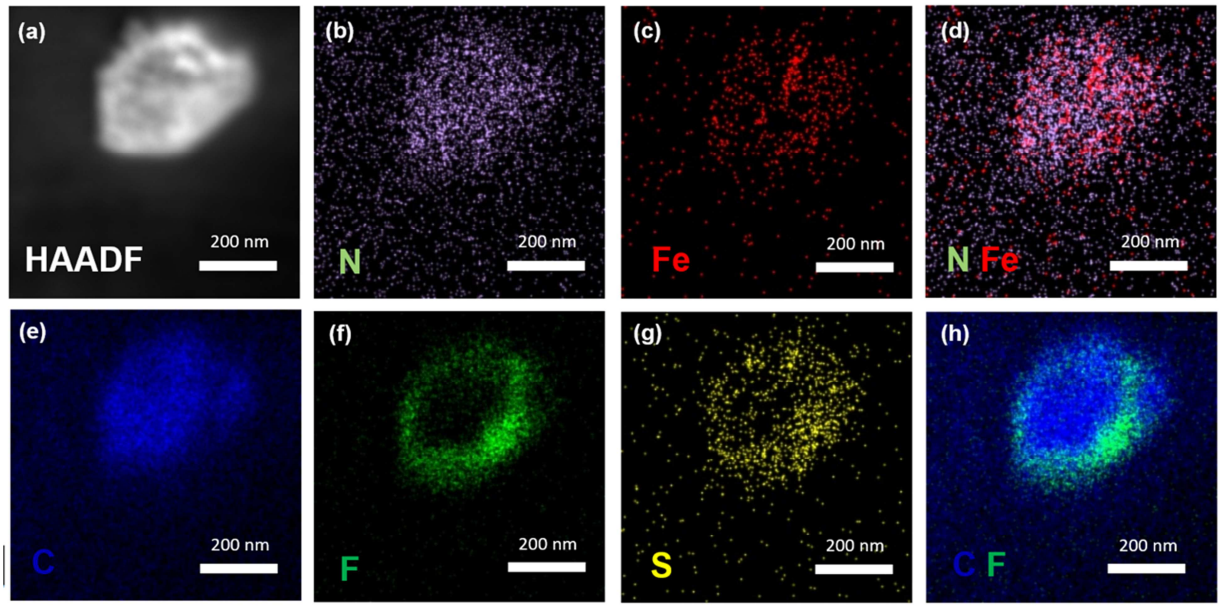

Figure 6. **HAADF STEM image (a) showing the cross-sectional view of a nanofiber. EDS maps of (b) nitrogen, N-purple (c) iron, Fe-red (d) nitrogen and iron, Fe-red and N-purple (e) carbon, C-blue (f) fluorine, F-green (g) sulfur, S-yellow (h) carbon and fluorine overlays, C-blue and F-green, demonstrating the elemental distribution across the fiber diameter.**

To visualize ionomer distribution across the fiber diameter, the fibers were cross-sectioned using ultramicrotomy and the elemental distributions examined using STEM/EDS mapping. The nitrogen (N), iron (Fe) carbon (C) and iron-carbon (FeC) maps in Fig 6. b-e shows the composition and distribution of nitrogen-factionalized transition metal active sites within PGM-Free nanofibers , where as the fluorine (F), sulfur, (S) and fluorine-carbon (FC)

maps in Fig. 6 f-h show the distribution of Nafion's fluorinated backbone and sulfonic groups across the nanofibers.

As seen, the fluorine distribution across the PGM-free nanofibers shown in Fig. 6f clearly illustrates that ionomer and Fe-N-C catalyst within the fiber diameter are nearly conformally covered with a ca. 50 nm ionomer thin-film. Moreover, an overlapping sulfur (Fig. 6g) and nitrogen distribution (Fig. 6b) indicates that the sulfonic groups in the ionomer are also most likely interacting with the nitrogen moieties in the PGM-free fibers. Previous studies have also corroborated enhanced SO^{3-} sulfonic group interactions in ionomers with pyridinic-N and pyrrolic-N nitrogen moieties in PGM-Free electrodes.[21,45] Hence, although the interior of the fiber is not completely isolated, the majority of the ionomer-catalyst interactions are still limited to the exterior of the fiber due to improved contact with the ionomer thin film as shown in the fluorine and carbon distribution in Fig 6(h).

According to TEM analysis, the sulfur (S) and fluorine (F) distribution across the PGM-free nanofibers indicates a close association between catalyst matrix, active sites and proton conducting ionomer, which correlates well with the normalized capacitance, N_C data. Though the interior of the fiber remains in limited contact with the ionomer, a thin (ca. 50 nm) ionomer layer distributed across the entirety of catalyst layer surface in the nanofiber electrode will be able to provide sufficient ionic contact regardless of the surrounding water content.

A plausible explanation of this uniform ionomer coating, and good mixing of catalyst and binder with a thin and uniform coating of ionomer on all catalyst particles could be attributed to the ionomer interaction with the nitrogen-functionalized groups, as well as the hydrophilic PAA under electrostatic sheer forces under a high voltage, which could affect and altered the ionomer-

carbon interactions relative to their viscosities, there-by dictating its arrangement and distribution across the fiber dimensions. This is mainly due to the micellar dispersion of Nafion in alcohol/water mixtures,[46] which will not electrospin into well-formed fibers, unless a suitable carrier polymer is added to the electrospinning solution.[47]

Though it is not clearly understood how electrospinning different blends of ionomer, catalyst, carrier polymer and solvent mixtures determine the final morphological properties of the fiber structure, gaining further insights into the electrochemical properties of PGM-free nanofiber electrodes is imperative, and needed for quantifying these interactions between the carbons, binders and solvents being utilized in order to improve and dictate the nanofiber electrode structures.

3.5 Bulk Transport and Impedance Spectroscopy.

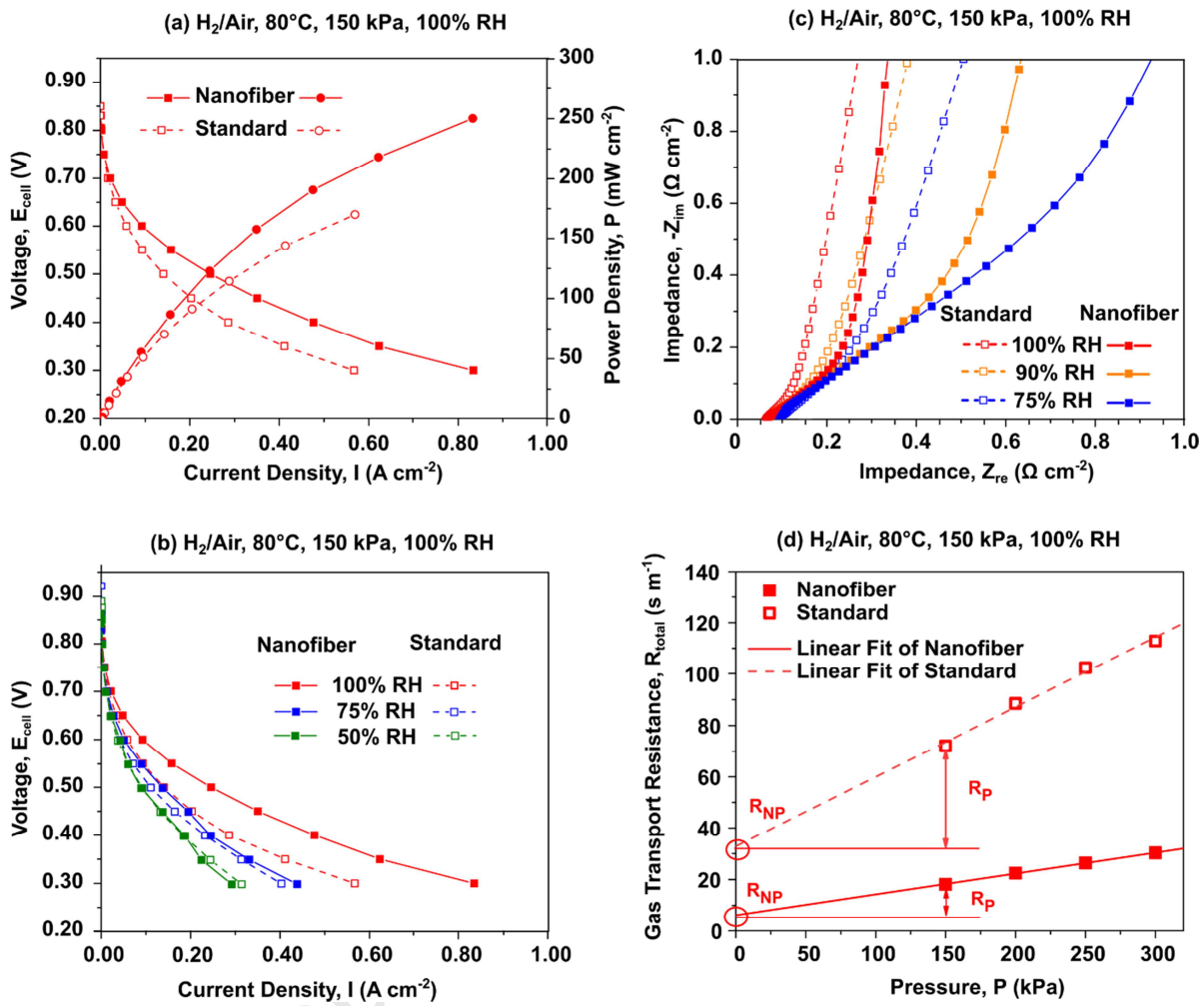

Figure 7. **(a) Fuel cell polarization curves for 5 cm^2 MEAs with PGM-free (■) nanofiber and (□) standard electrodes with a loading of 3 mg cm^{-2} operated in H_2/Air at 80°C, 150 kPa, and 100% RH and (b) 50, 75 and 100% RH; (c) Nyquist plot showing change in the fuel cell impedance with frequency as a function of relative humidity; (d) gas transport resistances in standard and nanofiber electrodes showing (d) total gas transport resistance, R_{total} comprising of both non-pressure dependent (R_{NP}) and pressure dependent (R_P) transport resistances at as a function of pressure at 100% RH, 80°C.**

Achieving high FC performances, requires a well-developed electrode structure with a network for electronic conduction through the carbon-based electrocatalyst, proton transport through ionomer films, and reactant gas supply through electrode and electrocatalyst pores. Fig. 7a and b show the performance of the electrospun and standard PGM-free electrodes in H_2/Air fuel cells. Under fully humidified conditions (100% RH), the nanofiber MEA demonstrated improved performance in comparison to the standard MEA. Under identical current densities, the nanofiber electrodes show a great improvement when compared to standard painted electrodes. Moreover, the PGM-free nanofiber electrodes attain a peak power density of ~240 mW cm^{-2} whereas the standard electrodes reach only a peak power density of ~175 $mW \cdot cm^{-2}$ in H_2/Air.

These improvements can arise from either improved proton or gas phase transport. However, these two transport phenomenas are independent – and we have a limited understanding of these transport processes particularly in PGM-free and nanofiber electrodes. O_2 transport can be facilitated through the macroporous voids between the interconnected nanofibers. However, proton (H^+) conduction to active sites is significantly reduced when not in contact with ionomer. This is especially true under drier conditions where capillary condensation is diminished resulting in a loss of ionic conductivity through micro and meso-pores. [48] Moreover, in practical PEMFCs, proton conduction resistances within the catalyst layer vary according to the distance from the interface between the polymer membrane and the CL.[49] In order to gain a better understanding of our electrode structures, well established electrochemical in-situ diagnostic measurements such as electrochemical impedance spectroscopy (EIS) and hydrogen-limiting current diagnostics[34] were utilized for characterizing and decoupling bulk-electrode gas transport and proton transport-dependent performances in the PGM-free catalyst layers.

In this study, the proton resistivity of the standard and nanofiber electrodes was measured using EIS, where AC impedances were collected and analyzed using Nyquist plots to determine the ohmic resistances in the catalyst layers.[50] Fig. 7c shows the overall cell impedance under different relative humidity. Most EIS data are analyzed using a graphical approach, that describes variation in ionic resistances inside electrodes using a transmission line model, where the Nyquist plots would have 45°-sloped lines at high frequencies. However, the Nyquist plots in these PGM-free electrodes have a curvature, which makes the determination of catalyst layer resistance in thick-PGM free electrodes difficult to gauge. Nonetheless, a *qualitative* comparison can still be made, where we see an increasing impedance with decreasing relative humidity, with the upsurge being more prominent in nanofiber electrodes.

An increased impedance is indicative of a higher proton resistance, as proton transport is hindered and rendered inaccessible to active sites at lower water content and humidity. Though the trends are similar in both the electrodes, - i.e. increasing impedance due to lower proton transport in dry conditions – it is more significant in the nanofiber electrodes, most likely due to the presence of the carrier polymer and proximity of the ionomer near the fiber surface as opposed to being more well-connected in the electrode bulk. Moreover, the PAA binder in the nanofiber electrodes could also be decreasing proton conductivity by a proportion greater than its volume fraction. It is also likely that the increase in proton resistivity might be due to electrospun electrode's more macroporous structure while the proton conductivity itself would be comparable, although the effect of macropores and presence of PAA on proton resistance cannot be independently decoupled using EIS.

Nevertheless, it is clear that an optimal balance between proton conductivity, binder content, electrode thickness and ionomer/carbon ratio needs to be optimized for the type of

carrier polymer being utilized in order to compensate for binder conductivity, and this will be the focus of our future studies. At present however, the distribution of ionomer across the catalyst layer thickness cannot necessarily be inferred from proton resistivity measurements alone, so further correlations can be deduced from bulk gas transport measurements using limiting current experiments.

Previous studies have utilized the oxygen limiting current measurement technique for determining mass transport resistances arising from constituent materials and cell components.[51,52] However, this method can be difficult to apply to PGM-free based electrodes, where ohmic contributions mainly dominate over transport phenomena. In this condition, hydrogen could be used as the molecular probe for evaluating mass transport resistance instead of oxygen. [53]

In this work, the hydrogen limiting current measurement approach was implemented for determining in situ mass transport resistances through the bulk of catalyst layer in the standard and nanofiber electrodes, via a complementary approach integrating a platinum black (PtB) sensor layer into the membrane electrode assembly (MEA) as described previously.[34,38] The PtB sensor platform enables determination of mass transport resistance through the entire electrode thickness in PGM-free catalyst layers using a transport probe molecule (H_2) that reacts on the PtB layer at the boundary of the porous catalyst layer, as the PGM-free catalyst used in this work is not electrochemically active to hydrogen at the operating conditions of interest.

The nanofiber and standard painted CCLs were deposited onto the PtB sensor layer as described in section 2.4 and the hydrogen oxidation reaction (HOR) limiting current densities were obtained.(Fig. S4) For determining the total transport resistance (R_{total}) for PGM-free

catalyst layers only, a cell was built with a PtB layer and one diffusion medium (DM) and tested under the same condition. By subtracting the resistance of the PtB|DM platform at each pressure and RH condition, R_{total} was obtained for PGM-free electrode only according to Equation 2.

$$R_{measured} = R_b + R_{total} = \frac{nFC_{H_2,channel}}{lim,ob \quad x \quad CV} \qquad [2]$$

Where $R_{measured}$ is the measured transport resistance through the entire cell, R_b is the background resistance in the absence of a PGM-free catalyst layer, n is the number of electrons transferred by reaction, F is Faraday's constant, $C_{H_2,channel}$ is the H_2 concentration in the flow field channel, $i_{l\ m,ob}$ is the measured limiting current, i_x is the crossover current, and i_{CV} is the background capacitive current flowing N_2 on the cathode. R_{total} for the electrodes as a function of pressure at 100% RH is shown in Fig. 8a. R_{total} is the sum of two separate contributions: pressure-dependent resistance (R_P) from molecular diffusion and pressure-independent resistance (R_{NP}) due to Knudsen diffusion through smaller pores in combination with solid-state diffusion through ionomer films. These values can be derived from the linear fitting of R_{total} as a function of pressure, where R_{NP} is the ordinate intercept of the linear trend line of R_{total} and R_P the remaining component, shown in Fig 8b. and Fig. 8c respectively.

As seen in Fig. 8, the nanofiber electrode showed not only a lower R_{total} (Fig. 8a) when compared to the standard electrode, but also a near zero dependence on RH. Since R_{NP} and R_P occur both in parallel and series within the electrode structure, any effect of increased ionomer swelling, as water uptake increases with RH, would result in a significant reduction of electrode pore sizes in the Knudsen regime (reductions of 10-20 nm) and a subsequent increased path length for molecular diffusion. However, the increased inter-fiber macro-porosity of the

nanofiber electrodes limit the effect of thin-film ionomer swelling at high RH,[54] thereby minimizing the effect of perceived cathode flooding.

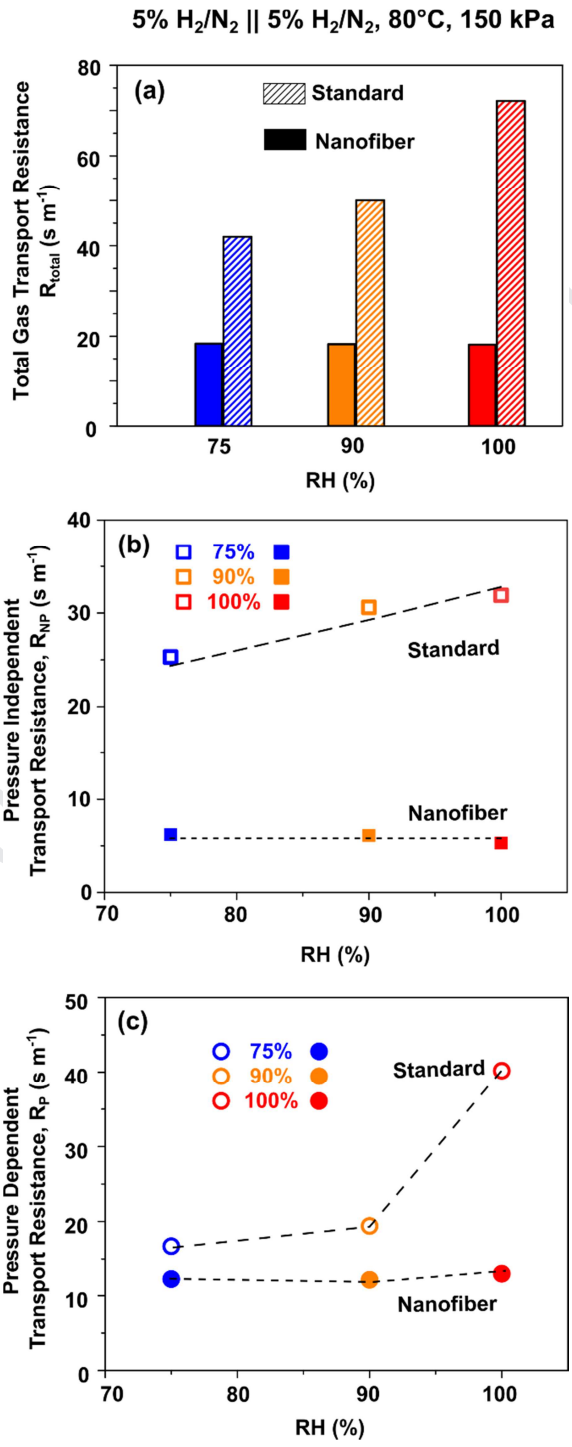

Figure 8. **(a) Pressure independent, R_{NP} (b) Pressure dependent, R_P and (c) Bulk electrode, R_{total} transport resistance measurement for standard and nanofiber electrode as a function of relative humidity.**

Fig. 8b shows that the standard electrodes have a higher R_{NP} component compared to the nanofiber electrode, which increases as a function of RH. For the standard electrodes, increasing RH leads to ionomer water uptake and swelling,[32] reducing the diameter of intra-fiber pores where Knudsen diffusion dominates, causing a detrimental effect on the R_{NP} component in standard electrodes, as depicted in Fig. 9. Previous studies have shown that blocking of pores by ionomer aggregates can substantially hinder oxygen mass transport through the electrode, especially when the ionomer is swelling due to high water uptake.[55]

The reduced bulk-electrode transport resistance in the nanofiber in comparison to the standard electrode clearly explains the improved H_2/Air performance observed at 100% RH in Fig. 7b, where the improved transport of gas phase reactant is increasingly offset by the decreased proton conductivity at low RH for the nanofiber electrodes.

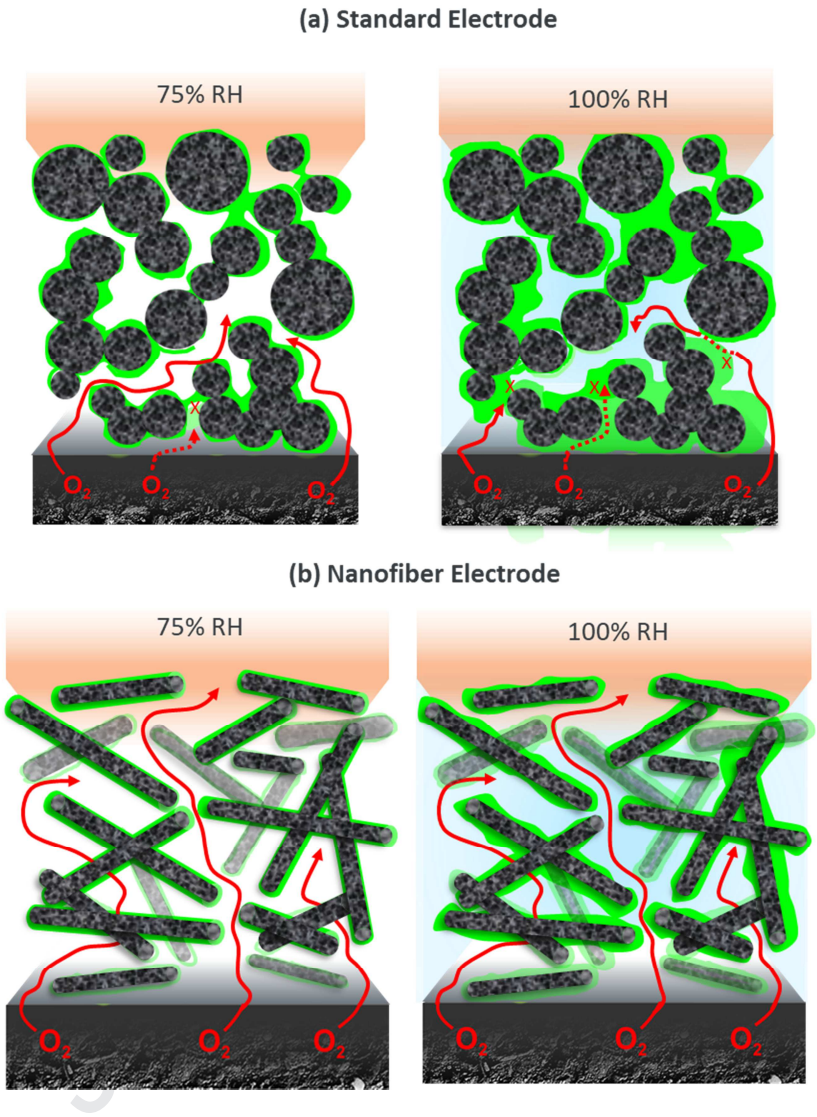

Figure 9. **Schematic representation of ionomer distribution and gas transport at high and low RH in (a) standard and (b) nanofiber electrode layers.**

4. Conclusion

It is plausible to overcome transport limitations associated with thicker PGM-free electrodes through tailoring alternative electrode architectures aimed at maximizing the bulk electrode transport properties, whilst simultaneously improving H_2-O_2/Air fuel cell performance and active site accessibility. Electrospinning as a technique has been shown to be capable of fabricating

materials with advantages of very high ratio of surface area to volume, improved macro-porosity as well as reduced bulk gas transport resistances. The creation of particle/polymer nanofiber mat electrodes via electrospinning represents an entirely different strategy for maximizing active site accessibility, while maintaining high power output in a hydrogen/air fuel cell.

In this work, PGM-free nanofibers with an average diameter of 450-700 nm were prepared by electrospinning a mixture of pyrolyzed Nicarbazine derived Fe-N-C catalyst, Nafion ionomer and a carrier polymer (Poly Acrylic acid (PAA). The PGM-dree nanofibers were conformally covered with thin film of proton conducting ionomer which reduced its dependency on liquid water for ionic accessibility, and also an increased electric double layer capacitance resulting from the increased break-up of large aggregates due to particle shearing under the applied electric field during the electrospinning process, leading to increased electrochemically accessible (carbon) surface area.

The improvements in H_2/Air performance under both dry and wet conditions can be directly correlated to an increased contact of active sites with reactant gases through the porous network of nanofibers providing a sufficient number of pathways for effective proton and electron conduction. The inter-fiber porosity is also crucial for release of cathode product water which gives the nanofiber electrodes an ability to provide better water management under saturated conditions at high current densities.

The bulk gas transport resistances in the nanofiber electrode were also significantly lower due to reduced contributions of both molecular and Knudsen diffusion through pores, where the molecular diffusion pathway of O_2 in the nanofiber electrodes was less tortuous due to the conformal ionomer coverage and macroporous network. It should be noted that while the bulk

gas phase transport resistances are lowered in nanofiber electrodes, there is also an increase in proton resistance. However, a combined effect of the improved gas transport, improved active site accessibility, as well as sufficient ionomer content and distribution was large enough to compensate for lower protonic conductivity. These results indicate that the large differences in the H_2/Air performance are not reflected in the measured proton conduction resistance in the different cathodes, but are strongly dependent on the bulk gas transport.

The results from this experimental approach not only offer the guidance of transport properties and the role of ionomer loading played in the PGM-free electrodes but also increase our understanding of achieving an optimized performance for a PGM-free catalyst at an MEA level. Improved device-level understanding of mass transport limitations in the catalyst coated layer can help accelerate deployment of low cost, PGM-free PEMFCs and be useful to guide ongoing research and development in both catalyst synthesis and membrane electrode assembly fabrication. In the near future, hybrid composites and the effects of both ionomer and binder composition on electrode morphology, along with associated novel physico-chemical properties will be explored. Ultimately, this approach may enable the incorporation of PGM-free catalysts and electrodes into next-generation fuel cells. This approach could also expanded to other carbon-based catalytic applications, such as electrolyzers and Li-air batters, where easy access to active sites through effective mass transfer is essential.

5. Acknowledgements

This work was authored in part by Alliance for Sustainable Energy, LLC, the manager and operator of the National Renewable Energy Laboratory for the U.S. Department of Energy (DOE) under Contract No. DE-AC36-08GO28308. Research performed as part of the Electrocatalysis Consortium (ElectroCat), established as part of the Energy Materials Network, which is supported by the U.S. Department of Energy, Office of Energy Efficiency and Renewable Energy, Fuel Cell Technologies Office (FCTO). While we do not endorse any materials presented in this study, we wish to thank Alexey Serov and Barr Zulevi of Pajarito Powders LLC for the use of their electrocatalysts. The views expressed in the article do not necessarily represent the views of the DOE or the U.S. Government.

6. References.

(1) Gasteiger, H. A.; Marković, N. M. Just a Dream—or Future Reality? *Science* **2009**, *324* (5923), 48–49. https://doi.org/10.1126/science.1172083.

(2) Yoshida, T.; Kojima, K. Toyota MIRAI Fuel Cell Vehicle and Progress Toward a Future Hydrogen Society. *Electrochem. Soc. Interface* **2015**, 5.

(3) Chen, C.; Kang, Y.; Huo, Z.; Zhu, Z.; Huang, W.; Xin, H. L.; Snyder, J. D.; Li, D.; Herron, J. A.; Mavrikakis, M.; Chi, M.; More, K. L.; Li, Y.; Markovic, N. M.; Somorjai, G. A.; Yang, P.; Stamenkovic, V. R. Highly Crystalline Multimetallic Nanoframes with Three-Dimensional Electrocatalytic Surfaces. *Science* **2014**, *343* (6177), 1339–1343. https://doi.org/10.1126/science.1249061.

(4) Stamenkovic, V. R.; Fowler, B.; Mun, B. S.; Wang, G.; Ross, P. N.; Lucas, C. A.; Marković, N. M. Improved Oxygen Reduction Activity on Pt3Ni(111) via Increased

Surface Site Availability. *Science* **2007**, *315* (5811), 493–497. https://doi.org/10.1126/science.1135941.

(5) Gasteiger, H. A.; Kocha, S. S.; Sompalli, B.; Wagner, F. T. Activity Benchmarks and Requirements for Pt, Pt-Alloy, and Non-Pt Oxygen Reduction Catalysts for PEMFCs. *Appl. Catal. B Environ.* **2005**, *56* (1), 9–35. https://doi.org/10.1016/j.apcatb.2004.06.021.

(6) Huang, X.; Zhao, Z.; Cao, L.; Chen, Y.; Zhu, E.; Lin, Z.; Li, M.; Yan, A.; Zettl, A.; Wang, Y. M.; Duan, X.; Mueller, T.; Huang, Y. High-Performance Transition Metal–Doped Pt3Ni Octahedra for Oxygen Reduction Reaction. *Science* **2015**, *348* (6240), 1230–1234. https://doi.org/10.1126/science.aaa8765.

(7) Thompson, S. T.; Papageorgopoulos, D. Platinum Group Metal-Free Catalysts Boost Cost Competitiveness of Fuel Cell Vehicles. *Nat. Catal.* **2019**, *2* (7), 558–561. https://doi.org/10.1038/s41929-019-0291-x.

(8) Thompson, S. T.; Wilson, A. R.; Zelenay, P.; Myers, D. J.; More, K. L.; Neyerlin, K. C.; Papageorgopoulos, D. ElectroCat: DOE's Approach to PGM-Free Catalyst and Electrode R&D. *Solid State Ion.* **2018**, *319*, 68–76. https://doi.org/10.1016/j.ssi.2018.01.030.

(9) The US Department of Energy (DOE) Energy Efficiency and Renewable Energy. Fuel Cell Multi-Year Research, Development and Demonstration Plan. https://www1.eere.energy.gov/hydrogenandfuelcells/mypp/pdfs/fuel_cells.pdf.

(10) DOE Technical Targets for Polymer Electrolyte Membrane Fuel Cell Components https://www.energy.gov/eere/fuelcells/doe-technical-targets-polymer-electrolyte-membrane-fuel-cell-components (accessed Jun 2, 2019).

(11) Bashyam, R.; Zelenay, P. A Class of Non-Precious Metal Composite Catalysts for Fuel Cells. *Nature* **2006**, *443* (7107), 63–66. https://doi.org/10.1038/nature05118.

(12) Jasinski, R. A New Fuel Cell Cathode Catalyst. *Nature* **1964**, *201* (4925), 1212–1213. https://doi.org/10.1038/2011212a0.

(13) Kabir, S.; Artyushkova, K.; Kiefer, B.; Atanassov, P. Computational and Experimental Evidence for a New TM–N 3 /C Moiety Family in Non-PGM Electrocatalysts. *Phys. Chem. Chem. Phys.* **2015**, *17* (27), 17785–17789. https://doi.org/10.1039/C5CP02230D.

(14) Chung, H. T.; Cullen, D. A.; Higgins, D.; Sneed, B. T.; Holby, E. F.; More, K. L.; Zelenay, P. Direct Atomic-Level Insight into the Active Sites of a High-Performance PGM-Free ORR Catalyst. *Science* **2017**, *357* (6350), 479–484. https://doi.org/10.1126/science.aan2255.

(15) Zhang, H.; T. Chung, H.; A. Cullen, D.; Wagner, S.; I. Kramm, U.; L. More, K.; Zelenay, P.; Wu, G. High-Performance Fuel Cell Cathodes Exclusively Containing Atomically Dispersed Iron Active Sites. *Energy Environ. Sci.* **2019**, *12* (8), 2548–2558. https://doi.org/10.1039/C9EE00877B.

(16) Wang, X.; Zhou, J.; Fu, H.; Li, W.; Fan, X.; Xin, G.; Zheng, J.; Li, X. MOF Derived Catalysts for Electrochemical Oxygen Reduction. *J. Mater. Chem. A* **2014**, *2* (34), 14064–14070. https://doi.org/10.1039/C4TA01506A.

(17) Pylypenko, S.; Mukherjee, S.; Olson, T. S.; Atanassov, P. Non-Platinum Oxygen Reduction Electrocatalysts Based on Pyrolyzed Transition Metal Macrocycles. *Electrochimica Acta* **2008**, *53* (27), 7875–7883. https://doi.org/10.1016/j.electacta.2008.05.047.

(18) Serov, A.; Artyushkova, K.; Atanassov, P. Fe-N-C Oxygen Reduction Fuel Cell Catalyst Derived from Carbendazim: Synthesis, Structure, and Reactivity. *Adv. Energy Mater.* **2014**, *4* (10), 1301735. https://doi.org/10.1002/aenm.201301735.

(19) Jaouen, F.; Herranz, J.; Lefèvre, M.; Dodelet, J.-P.; Kramm, U. I.; Herrmann, I.; Bogdanoff, P.; Maruyama, J.; Nagaoka, T.; Garsuch, A.; Dahn, J. R.; Olson, T.; Pylypenko, S.; Atanassov, P.; Ustinov, E. A. Cross-Laboratory Experimental Study of Non-Noble-Metal Electrocatalysts for the Oxygen Reduction Reaction. *ACS Appl. Mater. Interfaces* **2009**, *1* (8), 1623–1639. https://doi.org/10.1021/am900219g.

(20) Tylus, U.; Jia, Q.; Strickland, K.; Ramaswamy, N.; Serov, A.; Atanassov, P.; Mukerjee, S. Elucidating Oxygen Reduction Active Sites in Pyrolyzed Metal–Nitrogen Coordinated Non-Precious-Metal Electrocatalyst Systems. *J. Phys. Chem. C* **2014**, *118* (17), 8999–9008. https://doi.org/10.1021/jp500781v.

(21) Kabir, S.; Artyushkova, K.; Serov, A.; Atanassov, P. Role of Nitrogen Moieties in N-Doped 3D-Graphene Nanosheets for Oxygen Electroreduction in Acidic and Alkaline Media. *ACS Appl. Mater. Interfaces* **2018**, *10* (14), 11623–11632. https://doi.org/10.1021/acsami.7b18651.

(22) M. Barkholtz, H.; Liu, D.-J. Advancements in Rationally Designed PGM-Free Fuel Cell Catalysts Derived from Metal–Organic Frameworks. *Mater. Horiz.* **2017**, *4* (1), 20–37. https://doi.org/10.1039/C6MH00344C.

(23) Jaouen, F.; Proietti, E.; Lefèvre, M.; Chenitz, R.; Dodelet, J.-P.; Wu, G.; Chung, H. T.; Johnston, C. M.; Zelenay, P. Recent Advances in Non-Precious Metal Catalysis for Oxygen-Reduction Reaction in Polymer Electrolyte Fuel Cells. *Energy Environ. Sci.* **2010**, *4* (1), 114–130. https://doi.org/10.1039/C0EE00011F.

(24) Chen, Z.; Higgins, D.; Yu, A.; Zhang, L.; Zhang, J. A Review on Non-Precious Metal Electrocatalysts for PEM Fuel Cells. *Energy Environ. Sci.* **2011**, *4* (9), 3167–3192. https://doi.org/10.1039/C0EE00558D.

(25) Banham, D.; Ye, S. Current Status and Future Development of Catalyst Materials and Catalyst Layers for Proton Exchange Membrane Fuel Cells: An Industrial Perspective. *ACS Energy Lett.* **2017**, *2* (3), 629–638. https://doi.org/10.1021/acsenergylett.6b00644.

(26) Banham, D.; Choi, J.-Y.; Kishimoto, T.; Ye, S. Integrating PGM-Free Catalysts into Catalyst Layers and Proton Exchange Membrane Fuel Cell Devices. *Adv. Mater.* **2019**, *31* (31), 1804846. https://doi.org/10.1002/adma.201804846.

(27) Stariha, S.; Artyushkova, K.; Workman, M. J.; Serov, A.; Mckinney, S.; Halevi, B.; Atanassov, P. PGM-Free Fe-N-C Catalysts for Oxygen Reduction Reaction: Catalyst Layer Design. *J. Power Sources* **2016**, *326*, 43–49. https://doi.org/10.1016/j.jpowsour.2016.06.098.

(28) Yin, X.; Lin, L.; Chung, H. T.; Babu, S. K.; Martinez, U.; Purdy, G. M.; Zelenay, P. Effects of MEA Fabrication and Ionomer Composition on Fuel Cell Performance of PGM-Free ORR Catalyst. *ECS Trans.* **2017**, *77* (11), 1273–1281. https://doi.org/10.1149/07711.1273ecst.

(29) Jaouen, F.; Jones, D.; Coutard, N.; Artero, V.; Strasser, P.; Kucernak, A. Toward Platinum Group Metal-Free Catalysts for Hydrogen/Air Proton-Exchange Membrane Fuel Cells https://www.ingentaconnect.com/content/matthey/jmtr/2018/00000062/00000002/art00012# (accessed Nov 12, 2019). https://doi.org/info:doi/10.1595/205651318X696828.

(30) Kongkanand, A.; Subramanian, N. P.; Yu, Y.; Liu, Z.; Igarashi, H.; Muller, D. A. Achieving High-Power PEM Fuel Cell Performance with an Ultralow-Pt-Content Core–Shell Catalyst. *ACS Catal.* **2016**, *6* (3), 1578–1583. https://doi.org/10.1021/acscatal.5b02819.

(31) Komini Babu, S.; Chung, H. T.; Zelenay, P.; Litster, S. Resolving Electrode Morphology's Impact on Platinum Group Metal-Free Cathode Performance Using Nano-CT of 3D Hierarchical Pore and Ionomer Distribution. *ACS Appl. Mater. Interfaces* **2016**, *8* (48), 32764–32777. https://doi.org/10.1021/acsami.6b08844.

(32) Xie, J.; Xu, F.; Wood, D. L.; More, K. L.; Zawodzinski, T. A.; Smith, W. H. Influence of Ionomer Content on the Structure and Performance of PEFC Membrane Electrode Assemblies. *Electrochimica Acta* **2010**, *55* (24), 7404–7412. https://doi.org/10.1016/j.electacta.2010.06.067.

(33) Banham, D.; Kishimoto, T.; Zhou, Y.; Sato, T.; Bai, K.; Ozaki, J.; Imashiro, Y.; Ye, S. Critical Advancements in Achieving High Power and Stable Nonprecious Metal Catalyst–Based MEAs for Real-World Proton Exchange Membrane Fuel Cell Applications. *Sci. Adv.* **2018**, *4* (3). https://doi.org/10.1126/sciadv.aar7180.

(34) Star, A. G.; Wang, G.; Medina, S.; Pylypenko, S.; Neyerlin, K. C. Mass Transport Characterization of Platinum Group Metal-Free Polymer Electrolyte Fuel Cell Electrodes Using a Differential Cell with an Integrated Electrochemical Sensor. *J. Power Sources* **2020**, *450*, 227655. https://doi.org/10.1016/j.jpowsour.2019.227655.

(35) Li, J.; Brüller, S.; Sabarirajan, D. C.; Ranjbar-Sahraie, N.; Sougrati, M. T.; Cavaliere, S.; Jones, D.; Zenyuk, I. V.; Zitolo, A.; Jaouen, F. Designing the 3D Architecture of PGM-Free Cathodes for H2/Air Proton Exchange Membrane Fuel Cells. *ACS Appl. Energy Mater.* **2019**. https://doi.org/10.1021/acsaem.9b01181.

(36) Shui, J.; Chen, C.; Grabstanowicz, L.; Zhao, D.; Liu, D.-J. Highly Efficient Nonprecious Metal Catalyst Prepared with Metal–Organic Framework in a Continuous Carbon

Nanofibrous Network. *Proc. Natl. Acad. Sci.* **2015**, *112* (34), 10629–10634. https://doi.org/10.1073/pnas.1507159112.

(37) Slack, J.; Halevi, B.; McCool, G.; Li, J.; Pavlicek, R.; Wycisk, R.; Mukerjee, S.; Pintauro, P. Electrospun Fiber Mat Cathode with Platinum-Group-Metal-Free Catalyst Powder and Nafion/PVDF Binder. *ChemElectroChem* **2018**, *5* (12), 1537–1542. https://doi.org/10.1002/celc.201800283.

(38) Wang, G.; Osmieri, L.; Star, A. G.; Pfeilsticker, J.; Neyerlin, K. C. Elucidating the Role of Ionomer in the Performance of Platinum Group Metal-Free Catalyst Layer via in Situ Electrochemical Diagnostics. *J. Electrochem. Soc.* **2020**, *167* (4), 044519. https://doi.org/10.1149/1945-7111/ab7aa1.

(39) Engineering PGM-Free Electrodes to Facilitate Improved Performance for the Oxygen Reduction Reaction in Polymer Electrolyte Fuel Cells. *ECS Meet. Abstr.* **2019**. https://doi.org/10.1149/MA2019-02/32/1425.

(40) Li, G.; Anderson, L.; Chen, Y.; Pan, M.; Chuang, P.-Y. A. New Insights into Evaluating Catalyst Activity and Stability for Oxygen Evolution Reactions in Alkaline Media. *Sustain. Energy Fuels* **2017**, *2* (1), 237–251. https://doi.org/10.1039/C7SE00337D.

(41) Ferrandon, M.; Wang, X.; Kropf, A. J.; Myers, D. J.; Wu, G.; Johnston, C. M.; Zelenay, P. Stability of Iron Species in Heat-Treated Polyaniline–Iron–Carbon Polymer Electrolyte Fuel Cell Cathode Catalysts. *Electrochimica Acta* **2013**, *110*, 282–291. https://doi.org/10.1016/j.electacta.2013.03.183.

(42) Li, J.; Ghoshal, S.; Liang, W.; Sougrati, M.-T.; Jaouen, F.; Halevi, B.; McKinney, S.; McCool, G.; Ma, C.; Yuan, X.; Ma, Z.-F.; Mukerjee, S.; Jia, Q. Structural and Mechanistic

Basis for the High Activity of Fe–N–C Catalysts toward Oxygen Reduction. *Energy Environ. Sci.* **2016**, *9* (7), 2418–2432. https://doi.org/10.1039/C6EE01160H.

(43) Osmieri, L.; Ahluwalia, R. K.; Wang, X.; Chung, H. T.; Yin, X.; Kropf, A. J.; Park, J.; Cullen, D. A.; More, K. L.; Zelenay, P.; Myers, D. J.; Neyerlin, K. C. Elucidation of Fe-N-C Electrocatalyst Active Site Functionality via in-Situ X-Ray Absorption and Operando Determination of Oxygen Reduction Reaction Kinetics in a PEFC. *Appl. Catal. B Environ.* **2019**, *257*, 117929. https://doi.org/10.1016/j.apcatb.2019.117929.

(44) Karan, K. Interesting Facets of Surface, Interfacial, and Bulk Characteristics of Perfluorinated Ionomer Films. *Langmuir* **2019**, *35* (42), 13489–13520. https://doi.org/10.1021/acs.langmuir.8b03721.

(45) Ott, S.; Orfanidi, A.; Schmies, H.; Anke, B.; Nong, H. N.; Hübner, J.; Gernert, U.; Gliech, M.; Lerch, M.; Strasser, P. Ionomer Distribution Control in Porous Carbon-Supported Catalyst Layers for High-Power and Low Pt-Loaded Proton Exchange Membrane Fuel Cells. *Nat. Mater.* **2020**, *19* (1), 77–85. https://doi.org/10.1038/s41563-019-0487-0.

(46) Loppinet, B.; Gebel, G.; Williams, C. E. Small-Angle Scattering Study of Perfluorosulfonated Ionomer Solutions. *J. Phys. Chem. B* **1997**, *101* (10), 1884–1892. https://doi.org/10.1021/jp9623047.

(47) Ballengee, J. B.; Pintauro, P. N. Morphological Control of Electrospun Nafion Nanofiber Mats. *J. Electrochem. Soc.* **2011**, *158* (5), B568–B572. https://doi.org/10.1149/1.3561645.

(48) Cetinbas, F. C.; Ahluwalia, R. K.; Kariuki, N. N.; Andrade, V. D.; Myers, D. J. Effects of Porous Carbon Morphology, Agglomerate Structure and Relative Humidity on Local Oxygen Transport Resistance. *J. Electrochem. Soc.* **2020**, *167* (1), 013508. https://doi.org/10.1149/2.0082001JES.

(49) Mérida, W.; Harrington, D. A.; Le Canut, J. M.; McLean, G. Characterisation of Proton Exchange Membrane Fuel Cell (PEMFC) Failures via Electrochemical Impedance Spectroscopy. *J. Power Sources* **2006**, *161* (1), 264–274. https://doi.org/10.1016/j.jpowsour.2006.03.067.

(50) Yuan, X.; Sun, J. C.; Wang, H.; Zhang, J. AC Impedance Diagnosis of a 500W PEM Fuel Cell Stack: Part II: Individual Cell Impedance. *J. Power Sources* **2006**, *161* (2), 929–937. https://doi.org/10.1016/j.jpowsour.2006.07.020.

(51) Baker, D. R.; Caulk, D. A.; Neyerlin, K. C.; Murphy, M. W. Measurement of Oxygen Transport Resistance in PEM Fuel Cells by Limiting Current Methods. *J. Electrochem. Soc.* **2009**, *156* (9), B991–B1003. https://doi.org/10.1149/1.3152226.

(52) Kabir, S.; Myers, D. J.; Kariuki, N. N.; Park, J.; Wang, G.; Baker, A.; Macauley, N.; Mukundan, R.; More, K. L.; Neyerlin, K. C. Elucidating the Dynamic Nature of Fuel Cell Electrodes as a Function of Conditioning: An Ex-Situ Materials Characterization and In-Situ Electrochemical Diagnostic Study. *ACS Appl. Mater. Interfaces* **2019**. https://doi.org/10.1021/acsami.9b11365.

(53) Spingler, F. B.; Phillips, A.; Schuler, T.; Tucker, M. C.; Weber, A. Z. Investigating Fuel-Cell Transport Limitations Using Hydrogen Limiting Current. *Int. J. Hydrog. Energy* **2017**, *42* (19), 13960–13969. https://doi.org/10.1016/j.ijhydene.2017.01.036.

(54) Kusoglu, A.; Dursch, T. J.; Weber, A. Z. Nanostructure/Swelling Relationships of Bulk and Thin-Film PFSA Ionomers. *Adv. Funct. Mater.* **2016**, *26* (27), 4961–4975. https://doi.org/10.1002/adfm.201600861.

(55) Orfanidi, A.; Rheinländer, P. J.; Schulte, N.; Gasteiger, H. A. Ink Solvent Dependence of the Ionomer Distribution in the Catalyst Layer of a PEMFC. *J. Electrochem. Soc.* **2018**, *165* (14), F1254–F1263. https://doi.org/10.1149/2.1251814jes.

Author Bio-sketch:

Sadia Kabir is a Postdoctoral Researcher in the Chemistry and Nanoscience Center at the National Renewable Energy Laboratory. She received her Ph.D. in Chemical Engineering from the University of New Mexico in 2017. During her graduate study, she worked on the synthesis and characterization of hierarchically porous nitrogen-functionalized templated electrocatalysts for energy conversion and environmental applications. Her current research focuses on the development of novel catalyst layer architectures for platinum and platinum group metal-free (PGM-free) fuel cell electrodes and elucidating their reaction kinetics and transport phenomena using ex-situ characterization and in-situ electrochemical diagnostics.

Guanxiong Wang obtained his Ph.D. in Chemical Engineering in 2016 from the Illinois Institute of Technology. He is now a Postdoctoral Researcher working in the Chemistry and Nanoscience Center at the National Renewable Energy Laboratory, USA. His main research interests are PGM and PGM-free catalysts development for oxygen reduction reaction, electrochemical reactions kinetics, and electrochemical energy conversion. He is also expertized on electrode structure design and polymer electrolyte fuel cell electrodes test and characterization. He is the author of more than 20 publications between peer-reviewed papers and book chapters.

Samantha Medina is a 3rd year PhD student in the Materials Science program at the Colorado School of Mines. Sam earned her B.S. from the University of Tennessee, Knoxville in Material Science and Engineering. Sam is a recipient of the GEM fellowship and is currently involved in projects in collaboration with NREL researchers in which she utilizes electron microscopy to study the various interfaces that exist in a fuel cell, including catalyst/ionomer, catalyst layer/membrane and catalyst layer/gas diffusion media. Sam is serving as the vice-president for the Mines student chapter of the Electrochemical Society (ECS) for the 2019-2020 school year.

Guido Bender is a senior scientist in the Chemistry and Nanoscience Center in the Electrochemical Engineering & Materials Chemistry Group of the National Renewable Energy Laboratory. He received his Ph.D. in Electrical Engineering from the Technical University of Munich and has over 15 years of experience in PEM fuel cell research with a focus on spatial diagnostics and contaminant impacts. Recently he has been involved in various aspects of low temperature electrolysis R&D.

Svitlana Pylypenko is an Assistant Professor in the Chemistry Department at the Colorado School of Mines. She is also involved in the interdisciplinary Materials Science Program at Mines and holds a joint appointment at the National Renewable Energy Laboratory. Svitlana received her B.S. and M.S in Chemistry and Chemical Engineering from the National Technical University of Ukraine and Ph.D. in Chemistry from the University of New Mexico. Svitlana's group at Mines investigates surfaces and interfaces of applied materials with the emphasis on building relationships between surface composition and structure, material properties and their performance.

Kenneth C. Neyerlin obtained his Ph.D. in Chemical Engineering in 2007 from the University of Rochester. He is a Senior Scientist in the Chemistry and Nanoscience Center in the Electrochemical Engineering & Materials Chemistry Group at the National Renewable Energy Laboratory. His research activities focus on the integration of materials for functional electrodes in electrochemical energy conversion technologies as well as the development and application of in-situ electrochemical diagnostics to elucidate the voltage loss contributions of fundamental processes.

Highlights

- Electrospun nanofiber electrode fabricated with conformal ionomer coverage and macroporous network
- Break-up of catalyst aggregates due to particle shearing under applied electric field
- Increased capacitance and accessibility to active sites under high & low RH conditions
- Inter-fiber voids in fiber mat significantly reduced bulk gas transport resistances
- Less tortuous O_2 molecular diffusion pathway and reduced Knudsen diffusion

The authors have no financial and personal relationships with other people or organizations to disclose that could inappropriately influence (bias) their work.

Author Credits

Sadia Kabir: Conceptualization, Methodology, Investigation, Writing – Original Draft and Data Curation. **Guanxiong Wang**: Investigation, Data Curation. **Samantha Medina:** Investigation, Data Curation. **Guido Bender:** Investigation, Resources. **Svitlana Pylypenko**: Supervision, Writing – review and editing. **K.C. Neyerlin**: Conceptualization, Supervision, Funding Acquisition, Writing – review and editing.